CrystEngComm

PAPER

View Article Online
View Journal | View Issue

Cite this: *CrystEngComm*, 2020, **22**, 1619

Covalently anchoring cobalt phthalocyanine on zeolitic imidazolate frameworks for efficient carbon dioxide electroreduction†

Zhongjie Yang,[ab] Xiaofei Zhang,[a] Chang Long,[ac] Shuhao Yan,[a] Yanan Shi,[a] Jianyu Han,[a] Jing Zhang,[d] Pengfei An,[d] Lin Chang[ab] and Zhiyong Tang *[ab]

Received 25th September 2019,
Accepted 13th November 2019

DOI: 10.1039/c9ce01517e

rsc.li/crystengcomm

Transformation of CO_2 into fuels has drawn great attention due to increasing carbon emission in recent years. Coupling metal–organic frameworks (MOFs) with molecular catalysts is a promising technique for boosting the efficiency of carbon dioxide capture and conversion. Herein, a CoTAPc–ZIF-90 hybrid catalyst is synthesized by decorating cobalt phthalocyanine on the outer surface of ZIF-90 through a Schiff base reaction. We demonstrate that the ZIF-90 substrate can cooperate with the cobalt active center to boost the electrocatalytic CO_2 reduction performance. CoTAPc–ZIF-90 shows a large current density of 13 mA cm^{-2} for effective conversion of CO_2 into CO in aqueous media at an overpotential of 0.86 V with a faradaic efficiency (FE) of 90%. What's more, the CoTAPc–ZIF-90 hybrid catalyst exhibits significantly higher catalyst stability compared with the free phthalocyanine molecule.

Introduction

Electrochemical reduction of CO_2 to chemical fuels is a promising way to alleviate the greenhouse effect and energy crisis, which would produce a range of carbon-based products, including C1 (CO, methane, methanol and formic acid), C2 (ethylene, ethanol and acetic acid) and longer alkyl chain products.[1–7] Electrocatalytic CO_2 reduction has good economic benefit, since it works in aqueous media under room temperature and ambient pressure conditions while the energy is supplied from reproducible sources such as wind and solar energy.[8] However, it remains highly challenging to design cost-efficient electrocatalysts with high catalytic activity, selectivity and durability.[9]

Chemical reactions often require catalysts, which are able to boost the reaction rate and improve the reaction selectivity. In traditional composite catalyst systems, the catalytic performance is directly related to their components and structure. Primary and assistant catalysts play important roles in affording active sites and improving catalytic activity, selectivity and stability, respectively.[10] As for electrochemical reduction of CO_2, molecular catalyst systems generally work either in organic media or at low current density and faradaic efficiency in aqueous solution, *i.e.* single component cobalt phthalocyanine exhibits 0.98 mA cm^{-2} at −1.15 V and a faradaic efficiency of 50%.[11] Meanwhile, a composite CO_2 reduction electrocatalyst, for instance, zeolitic imidazolate framework-8 (ZIF-8) with high overpotential and low faradaic efficiency (85% at η = 1.1 V *vs.* RHE), is developed *via* coupling with a strong electron-donating molecule, 1,10-phenanthroline. Interestingly, pristine zeolitic imidazolate framework-8 (ZIF-8, a major subclass of MOFs) shows no catalytic activity, and the sp^2 carbon atoms in the imidazolate ligand are determined to be the main catalytic sites after ligand doping.[12] Thus, design and application of composite catalysts will dramatically benefit CO_2 electrochemical reduction.

The cobalt phthalocyanine (CoPc) molecule on a conductive platform has been extensively studied as a hybrid electrocatalyst for the CO_2 reduction reaction. Meshitsuka *et al.*[13] reported for the first time that cobalt and nickel phthalocyanine graphite hybrid electrodes in aqueous electrolytes exhibited reduction peaks in the presence of CO_2. Recently, Wang *et al.*[14] showed a uniform distribution of CoPc molecules on carbon nanotubes *via* π–π interactions that possessed a faradaic efficiency of 90% at an overpotential of 0.52 V in aqueous solution, and the low durability (about 10 h at η = 0.52 V) was attributed to CoPc aggregation under electronic energy conditions due to the

[a] *CAS Key Laboratory of Nanosystem and Hierarchical Fabrication, CAS Center for Excellence in Nanoscience, National Center for Nanoscience and Technology, Beijing 100190, P. R. China*
[b] *University of Chinese Academy of Sciences, Beijing 100049, China*
[c] *School of Materials Science and Engineering, Harbin Institute of Technology, Harbin 150080, China*
[d] *Beijing Synchrotron Radiation Facility, Institute of High Energy Physics, Chinese Academy of Sciences, Beijing 100049, P. R. China*

† Electronic supplementary information (ESI) available: ^{1}H NMR spectrum, *ex situ* EXAFS data, CO and H_2 faradaic efficiency, Co element content and fitting parameters of Co K-edge EXAFS curves. See DOI: 10.1039/c9ce01517e

rather weak π–π interactions. Obviously, a suitable catalytic platform will play an important role in stabilizing molecular catalysts. MOFs with accurate molecular structures, well-dispersed pores and a high degree of crystallization have displayed great potential as catalytic platforms.[15] As examples, some MOFs were used as platforms for loading metal nanoparticles toward electrocatalytic CO_2 reduction.[16–24] Hupp *et al.*[25] reported that copper nanoparticles were embedded into a zirconium-based MOF by *in situ* electrochemical deposition, and the hybrid catalyst was electrocatalytically active with higher selectivity for hydrogen evolution over CO_2 reduction. Buonsanti *et al.*[26] indicated that silver nanoparticles embedded in an Al-PMOF ($[Al_2(OH)_2$-(TCPP)]) (tetrakis(4-carboxyphenyl)porphyrin (TCPP)) were in intimate contact with a conductive substrate to enhance electron transfer and suppress the hydrogen evolution reaction. However, the practical application would be limited by a low current density (j_{CO} = 0.15 mA cm^{-2}) and low faradaic efficiency (FE_{CO} = 60%).

To improve the performance of molecular catalysts in an electrochemical CO_2 reduction system, herein we report molecule–ZIF hybrid materials as effective catalysts, where cobalt tetraaminophthalocyanine (CoTAPc) is anchored onto the ZIF-90 outer surface through a Schiff base reaction for highly active, stable and selective CO_2 reduction to CO. Based on X-ray absorption spectroscopy results, the electronic structure of cobalt element in CoTAPc does not change after anchoring on the ZIF-90 outer surface. Significantly, ZIF-90 as a catalytic platform can not only capture CO_2 molecules from the electrolyte,[12] but also suppress the hydrogen evolution reaction.[27] As a result, the molecule–ZIF hybrid electrocatalyst selectively reduces CO_2 to CO with a large faradaic efficiency of 90%, a high current density of 13 mA cm^{-2} at η = 0.86 V, and excellent stability for at least 48 hours.

Experimental section

Chemical materials

All chemicals and solvents were used as received without any further purification. Urea, 4-nitrophthalonitrile and imidazole-2-carboxaldehyde (ICA) were purchased from Alfa Aesar. Sodium hydroxide (NaOH), sodium carbonate ($NaHCO_3$), potassium bromide (KBr), sodium sulfide ($Na_2S \cdot 9H_2O$) and ammonium molybdate ($H_8MoN_2O_4$) were bought from Macklin. Cobaltous chloride hexahydrate ($CoCl_2 \cdot 6H_2O$) and zinc nitrate hexahydrate ($Zn(NO_3)_2 \cdot 6H_2O$) were obtained from TCI (Shanghai) Development Co., Ltd. Anhydrous *N*,*N*-dimethylacetamide and anhydrous methanol were obtained from Innochem. Carbon dioxide (CO_2, 99.999%) and argon (Ar, 99.9999%) were supplied by Beijing Beiwen Gases Company. Ultrapure water (Millipore Milli-Q grade) with a resistivity of 18.2 MΩ was used in all experiments.

Synthesis of CoTAPc

CoTAPc was synthesized according to a previously reported method.[28] A uniformly mixed solid of 4-nitrophthalonitrile (1.9 g, 10.0 mmol), $CoCl_2 \cdot 6H_2O$ (0.6 g, 2.5 mmol), and urea (4.8 g, 80.0 mmol) and a small amount of ammonium molybdate catalyst were reacted in solid state at 160 °C for 5 h. The resulting crude product was ground and further stirred in aqueous HCl solution (1 M, 150 mL) and aqueous NaOH solution (1 M 150 mL) at 90 °C for 1 h, respectively. The residue was then filtered, washed with water, and dried under vacuum to obtain cobalt tetranitrophthalocyanine. The crude cobalt tetranitrophthalocyanine (0.75 g, 1.0 mmol) was then converted to CoTAPc by a reaction with $Na_2S \cdot 9H_2O$ (3.0 g, 37.0 mmol) in DMF (20 mL) at 70 °C for 4 h. The resulting solution was then poured into hot water (50 mL), and the precipitate was filtered and repeatedly washed with water until neutral. The product was dried under ambient vacuum conditions to get bluish-green CoTAPc.

Synthesis of ZIF-90

The ZIF-90 nanoparticles (NPs) were synthesized according to a previously reported hydrothermal method with slight modification.[29] $Zn(NO_3)_2 \cdot 6H_2O$ (2.69 mmol) and ICA (8.10 mmol) were added to 45 mL of DMF in a round bottom flask (150 mL). The resulting solution was sonicated for 15 min at room temperature and stirred at 80 °C for 4 h. After the solution was cooled to room temperature, methanol (45 mL) was quickly poured into the solution while applying vigorous stirring. After further stirring at room temperature for 60 min, the faint yellow solid products were recovered by centrifugation and washed several times with DMF and methanol (at least three times) to remove the excess reactants. Then, the resulting ZIF-90 sample was vacuum dried at 60 °C.

Synthesis of CoTAPc–ZIF-90

CoTAPc–ZIF-90 was synthesized according to a previous report.[29] 0, 5, 10, 20 or 30 mg of CoTAPc and 100 mg of ZIF-90 were dissolved in 5 mL of anhydrous methanol, respectively. A certain amount of CoTAPc was slowly added into ZIF-90 solution with stirring at room temperature. The resulting solution was vigorously stirred at 60 °C for 24 h. The dark green solid samples were isolated by centrifugation and washed with methanol three times. Then the hybrid products were vacuum dried at 60 °C and denoted as ZIF-90 (0 mg CoTAPc), ZIF-90-1 (5 mg CoTAPc), ZIF-90-2 (10 mg CoTAPc), ZIF-90-3 (20 mg CoTAPc) and ZIF-90-4 (30 mg CoTAPc), respectively.

Material characterization

A Rigaku D/MAX-TTRIII (CBO) X-ray powder diffractometer was used to get the powder X-ray diffraction (PXRD) patterns by using Cu Kα radiation (λ = 1.5418 Å). A Hitachi S8220 field emission scanning electron microscope (FESEM) was used to obtain the SEM images. Fourier transform infrared (FTIR) spectra were recorded on a Spectrum One in the spectral range of 450–4000 cm^{-1} using the KBr disk method. The Co content in different samples was determined by inductively

coupled plasma mass spectrometry (ICP-MS, Thermo Fisher Scientific). Nuclear magnetic resonance (NMR) spectra were recorded at 400 MHz with an Avance III Bruker Corporation instrument.

Electrochemical measurements

According to our previous work,[30] all electrochemical measurements were carried out using a CHI 660E potentiostat in a three-electrode configuration using hydrophobic carbon paper as the working electrode, a gauze platinum electrode as the counter electrode and Ag/AgCl (3.5 M KCl) as the reference electrode, respectively. All potentials were converted to reversible hydrogen electrode (RHE) values using the equation: E (*vs.* RHE) = E (*vs.* Ag/AgCl) + 0.205 V + 0.059 V × pH. For the preparation of the working electrode, 5 mg of catalyst and 30 μL of 5 wt% Nafion solution were dispersed in 1 mL of isopropanol and vigorously sonicated for 60 min to form a uniform catalyst ink. Then 150 μL of catalyst ink was uniformly dropped onto the carbon paper electrode with an area of 1 × 1 cm^2. Electrochemical measurements were carried out in a gas-tight two-compartment electrochemical cell with a piece of Nafion 117 cation-exchange membrane as the separator. A 0.5 M $NaHCO_3$ aqueous solution was used as the electrolyte and was purged with CO_2 (99.999%) at a speed of 20 mL min^{-1} for at least 30 minutes prior to electrolysis. Linear sweep voltammetry (LSV) measurements were performed at a scan rate of 10 mV s^{-1}. In order to determine the reduction products and their faradaic efficiency, bulk electrolysis was conducted at selected potentials (−0.77 V to −1.07 V *vs.* RHE). All electrochemical curves were obtained without iR corrections.

The evolved gaseous products were flowed into the gas-sampling loop of a gas chromatograph (GC, Shimadzu GC-2014C) equipped with a packed Molecular Sieve 5A capillary column (Agilent) and a Porapak Q column (Agilent, 80–100 mesh). Both a thermal conductivity detector (TCD) and flame ionization detector (FID) were installed on the GC to detect the evolved gaseous products. The liquid products were determined by ^{1}HNMR spectroscopy (Bruker Advance 400 spectrometer, 400 MHz) *via* water suppression using a presaturation method. A 500 μL electrolyte was mixed with 100 μL of D_2O, and 1.0 ppm dimethyl sulfoxide (DMSO) was added as the internal standard.

The faradaic efficiency (FE) was calculated from the concentration determined by GC using the following equation:

$$\mathrm{FE\%} = \mathrm{ppm} \times \text{flow rate} \times (nFp_0/\mathrm{RT}) \times (j_{\mathrm{Tot}})^{-1} \times 100$$

where ppm is the concentration of the gas (CO or H_2) determined by GC, n is the electron transfer number, F is the faradaic constant, p_0 is the pressure, T = 273.15 K and j_{Tot} is the total current density.

The partial current density of CO was calculated as follows:

$$j_{\mathrm{CO}} = j_{\mathrm{Tot}} \times \mathrm{FE}_{\mathrm{CO}}$$

where j_{CO} is the partial current density of CO, j_{Tot} is the total current density, and $\mathrm{FE}_{\mathrm{CO}}$ is the faradaic efficiency of CO.

The Tafel slope was calculated as follows:

$$\eta = a + b \times \log|j_{\mathrm{CO}}|$$

where η is the overpotential, a is the Tafel constant and b is the Tafel slope.

X-ray absorption data collection and analysis

Ex situ Co K-edge XAS was carried out under ambient conditions in transmission mode at beamline 1W1B of BSRF, using a Si (111) double-crystal monochromator. The storage ring of BSRF was operated at 2.5 GeV with a maximum current of 250 mA in decay mode. The energy was calibrated using a Co foil, and the intensity of the incident and transmitted X-rays was monitored by standard N_2-filled ion chambers. The powder samples (the pristine CoTAPc and ZIF-90-4) were pressed to a pellet to determine the best signal to noise ratio.

The obtained X-ray absorption fine structure (XAFS) data were processed in Athena (version 0.9.25) for background, pre-edge line and post-edge line calibrations. Then Fourier transformed fitting was carried out in Artemis (version 0.9.25). The k^2 weighted data, in the k-range of 3–12 $Å^{-1}$ and R range of 1–3 Å, were used for fitting. CoTAPc was used to calculate the simulated scattering paths. Four parameters, namely the coordination number, bond length, Debye–Waller factor and E_0 shift (CN, R, σ^2, and ΔE_0), were fitted without being fixed, constrained, or correlated.

Results and discussion

A series of CoTAPc–ZIF-90 hybrid catalysts are synthesized through a solvothermal reaction. ZIF-90 (100 mg) and CoTAPc (0, 5, 10, 20 or 30 mg) were dispersed into anhydrous methanol at 60 °C for 24 h to get ZIF-90, ZIF-90-1, ZIF-90-2, ZIF-90-3, and ZIF-90-4, respectively (see the Experimental section). The structures of the obtained CoTAPc–ZIF-90 hybrid catalysts were analyzed by XRD. As shown in Fig. 3A, all of the diffraction peaks are in good agreement with those

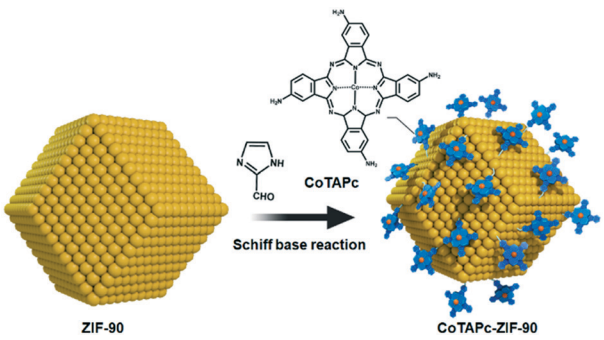

Fig. 1 Schematic illustration of the synthesis of CoTAPc–ZIF-90.

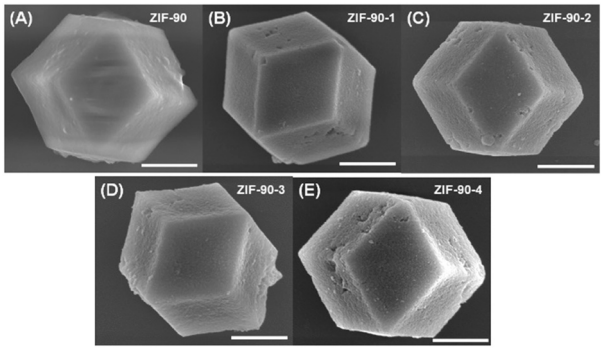

Fig. 2 SEM images of CoTAPc–ZIF-90 hybrid crystals at different added amounts of CoTAPc: (A) 0 mg, (B) 5 mg, (C) 10 mg, (D) 20 mg, and (E) 30 mg. Scale bars: 500 nm.

of pristine ZIF-90.[29] The morphology of the samples was characterized by SEM imaging. As shown in Fig. S3,† Zn, Co and N elements are uniformly distributed in ZIF-90-4 with a dodecahedron morphology. This result demonstrates that the CoTAPc units are uniformly distributed in the outer surface of ZIF-90. High-resolution SEM images show that the outer surface of pristine ZIF-90 is smooth and the CoTAPc–ZIF-90 hybrid catalysts become rougher with increasing amount of added CoTAPc (Fig. 2A–E). It is worth mentioning that the increased roughness of the electrodes benefits the improvement of the electrochemical performance.[29] FT-IR analysis was carried out to verify the formation of imine linkages through the Schiff base reaction. As shown in Fig. 3B, a new peak at 1620 cm^{-1} appears in the series of CoTAPc–ZIF-90 catalysts compared with pristine ZIF-90, which is assigned to the bending vibration of C═N, while the peak at 1671 cm^{-1} is ascribed to the stretching vibration of the remaining C═O in pristine ZIF-90.[29] The Co content is determined to be 0.46, 0.83, 1.81 and 2.61 wt% by inductively

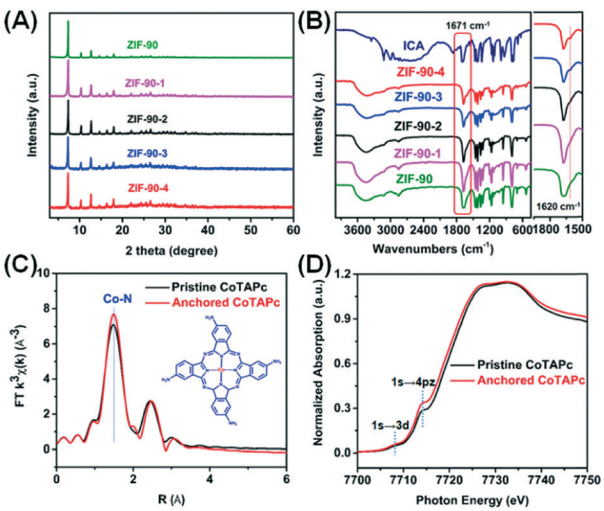

Fig. 3 XRD patterns (A) and FT-IR spectra (B) of CoTAPc–ZIF-90 hybrid crystals at different added amounts of CoTAPc (ZIF-90, ZIF-90-1, ZIF-90-2 ZIF-90-3, or ZIF-90-4). *Ex situ* EXAFS in *R* space (C) and Co K-edge XANES (D) of pristine CoTAPc and anchored CoTAPc.

coupled plasma (ICP) spectroscopy. These loadings are close to theoretical calculations of the Co content (Table S1†), demonstrating that all the added CoTAPc molecules are anchored on the outer surface of ZIF-90 (Fig. 1).

To further verify the structure of CoTAPc molecules on ZIF-90, the XAS technique was used to evaluate the electronic structure of the Co center (corresponding fitting results are shown in Fig. S2 and Table S2†). The Fourier transform (FT) *R* space of the extended X-ray absorption fine structure (EXAFS) spectra of the pristine and anchored CoTAPc is presented in Fig. 3C. Evidently, the EXAFS of the anchored CoTAPc at the Co K-edge are well consistent with those of pristine CoTAPc. Also, the X-ray absorption near edge spectra (XANES) of the Co K-edge energy of the pristine and anchored CoTAPc show nearly the same absorption shoulders (Fig. 3D). Note that the absorption shoulders in the XANES are the fingerprints of the Co–N_4 structure, where the first peak at 7708.6 eV is specified as the dipole forbidden 1s to 3d transition and the second peak at 7714.2 eV is attributed to the shakedown satellite 1s to $4p_z$ transition.[30,31] In other words, the CoTAPc molecules are successfully anchored onto the outer surface of ZIF-90, which might be a good platform to explore the electrochemical CO_2 reduction performance.

The electrochemical CO_2 reduction performance of the series of CoTAPc–ZIF-90 hybrid catalysts was evaluated in 0.5 M $NaHCO_3$ in an airtight electrochemical H-type cell (the compartments are separated by a piece of Nafion 117 cation-exchange membrane). All the CoTAPc–ZIF-90 hybrid (*i.e.*, ZIF-90, ZIF-90-1, ZIF-90-2, ZIF-90-3 and ZIF-90-4) catalysts were dropped cast onto carbon paper and subjected to examination. In this work, all the potentials were measured *vs.* the Ag/AgCl (3.5 M KCl) electrode and then converted to values *vs.* the reversible hydrogen electrode (RHE) without iR compensation.

The linear sweep voltammetry (LSV) curves of ZIF-90 and ZIF-90-4 were recorded at a scan speed of 10 mV s^{-1} in argon (Ar) and in CO_2 saturated 0.5 M $NaHCO_3$ solution (pH_{Ar} = 8.4 and pH_{CO_2} = 7.4), respectively. Notably, to reach a current density of 3 mA cm^{-2}, potentials of −1.16 V and −0.65 V *vs.* RHE are required for the pristine ZIF-90 and ZIF-90-4 in the CO_2 saturated $NaHCO_3$ solution, respectively (black and red curves in Fig. 4A). Correspondingly, the LSV curve of ZIF-90-4 in the Ar saturated $NaHCO_3$ solution shows a more negative potential of −0.97 V *vs.* RHE to reach 3 mA cm^{-2} (blue curve in Fig. 4A), which confirms the increased current density in the CO_2 saturated $NaHCO_3$ solution from catalyzing CO_2 conversion. Clearly, the CoTAPc–ZIF-90 hybrid catalyst has an excellent catalytic performance toward CO_2 reduction under aqueous conditions. Fig. 4B shows that with increasing amount of anchored CoTAPc, the electrochemical performance gradually becomes better. To further obtain an appropriate reduction potential of the series of molecule–ZIF hybrid catalysts for CO_2 reduction, all of the catalysts are electrolyzed for 2 hours at gradually increasing potential from −0.77 to −1.17 V *vs.* RHE. Generally, gaseous products (CO and H_2) are detected by gas chromatography (GC), and no

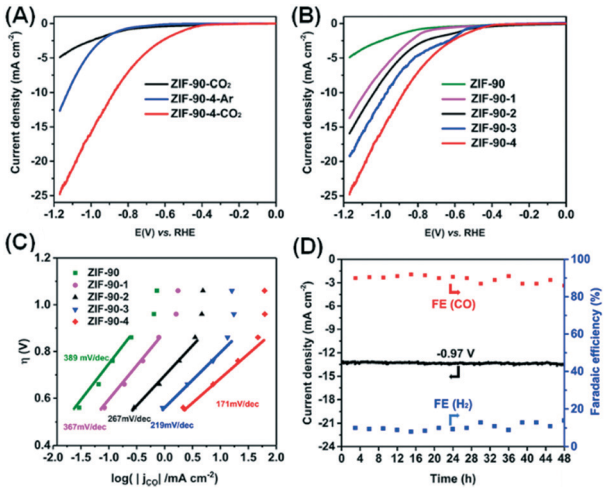

Fig. 4 (A) LSV curves of ZIF-90–CO_2, ZIF-90-4–Ar, and ZIF-90–CO_2. (B) LSV curves of CoTAPc–ZIF-90 hybrid crystals at different added amounts of CoTAPc in 0.5 M $NaHCO_3$ saturated with CO_2 at 10 mV s^{-1}, (ZIF-90, ZIF-90-1, ZIF-90-2, ZIF-90-3 and ZIF-90-4). (C) Tafel plots of ZIF-90, ZIF-90-1, ZIF-90-2, ZIF-90-3 and ZIF-90-4, respectively. (D) Chronoamperograms and faradaic efficiency of CO and H_2 for ZIF-90-4 over 48 h at −0.97 V *vs.* RHE.

liquid product is found by nuclear magnetic resonance (NMR) spectroscopy at the end of electrolysis (Fig. S4†). The relationship between selectivity and the applied potential is deduced for ZIF-90, ZIF-90-1, ZIF-90-2, ZIF-90-3 and ZIF-90-4 (Fig. S5A–E†). Remarkably, the highest CO faradaic efficiency (FE_{CO}) of 90% ± 1.5% for ZIF-90-4 is obtained at a potential of −0.97 V *vs.* RHE. As shown in Fig. 5, a more positive or negative potential would not largely set off water splitting, and hence the FE_{CO} of ZIF-90-4 remains beyond 65% in a wide range of preferences of CO_2 reduction. In sharp contrast, ZIF-90 shows a very low FE_{CO} (9.6% ± 2%–35.5% ± 3%) in the range of applied potentials. As shown in Fig. S7A,† when the applied potential is increased to −0.97 V, the CO faradaic efficiency continuously increases and reaches 81% and 90% for CoTAPc and ZIF-90-4, respectively. This result not only confirms that ZIF-90 could suppress the hydrogen evolution reaction, but also reveals that the high CO_2 RR activity of ZIF-90-4 mainly originates from Co-centered

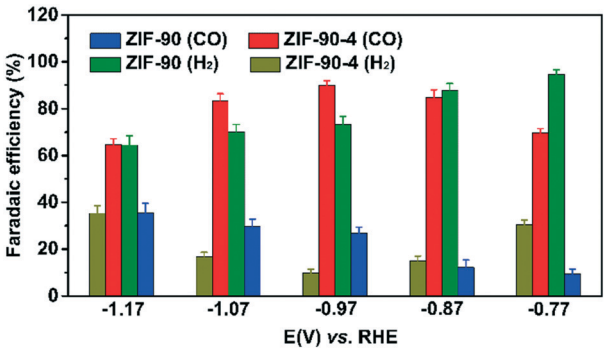

Fig. 5 CO and H_2 faradaic efficiency of ZIF-90-4 and ZIF-90-4 at different applied potentials.

macrocycles. Fig. S7B† shows that ZIF-90-4 has superior durability compared with CoTAPc, in good agreement with the fact that the anchored CoTAPc molecules are uniformly dispersed on the outer surface of ZIF-90 to provide the catalytic sites. As shown in Fig. S8† the specific activities of ZIF-90-1, ZIF-90-2, ZIF-90-3 and ZIF-90-4 are quantified by normalizing the CO partial current density with respect to the area of electrodes. At −0.97 V, the activity of ZIF-90-4 (12.85 mA cm^{-2}) is 2–22 times larger than that of the other four samples. What is more, ZIF-90-4 is the electrocatalyst with the highest content of CoTAPc, which is anchored on the outer surface of ZIF-90 through imine bonds. In the field of electrocatalytic carbon dioxide reduction, the functional groups adjacent to the active centers greatly affect the electrocatalytic performance.[32,33] In our case, ZIF-90-4 possesses the highest number of imine bonds and shows the best catalytic activity, mainly due to the increase of the local carbon dioxide concentration on the surface of the catalyst.[34,35]

To explore the possible electrochemical mechanism pathway, Tafel analysis is performed and data are plotted with the overpotential (η) against the logarithm of the steady-state CO partial current density [$\log(j_{CO})$] (Fig. 4C). The Tafel slope of ZIF-90-4 is calculated to be 171 mV dec^{-1} by linear fitting $\log(j_{CO})$ ranging from 0.57 V to 0.87 V. This value reveals that the initial electron transfer to CO_2 to form the $*COO^-$ intermediate is the possible rate-determining step.[36–41] The larger Tafel slope value of the other molecule–ZIF-90 hybrid catalysts is 219 mV dec^{-1}, 267 mV dec^{-1}, 367 mV dec^{-1} and 389 mV dec^{-1}, respectively, attributed to the mass transport limitations at a high current density. The durability of ZIF-90-4 is investigated at a potential of −0.97 V *vs.* RHE (Fig. 4D). The cathodic current density is maintained at −13 mA cm^{-2} for 48 h with negligible activity decay and the corresponding FE_{CO} is kept around 90% for the whole electrolysis period, demonstrating the superior durability of ZIF-90-4 compared with those of CoTAPc, CoPc/CNT,[14] CoPPc/CNT,[31] and defective polymeric-CoPc.[42]

Conclusion

In summary, we have successfully synthesized CoTAPc–ZIF-90 hybrid materials through a Schiff base reaction for high-performance electrocatalysis toward CO_2 reduction. Impressively, the ZIF-90-4 electrocatalyst (anchoring CoTAPc molecules as active moieties) exhibits a large current density of 13 mA cm^{-2} for electrochemical reduction of CO_2 to CO in aqueous solution at an overpotential of 0.86 V with a faradaic efficiency (FE) of 90%, while the excellent stability of ZIF-90-4 is distinguished with a negligible change within 48 hours of electrolysis. This study will open an avenue for immobilizing molecular catalysts on the surface of MOFs by covalent bond linkage to enhance catalyst durability as well as understand the synergistic effect of active sites and supports, which eventually guide the precise construction of highly efficient catalysts for energy conversion and storage.

Conflicts of interest

There are no conflicts of interest to declare.

Acknowledgements

The authors acknowledge financial support from National Key Basic Research Program of China (2016YFA0200700, Z. Y. T.), National Natural Science Foundation of China (21890381 and 21721002, Z. Y. T.), Frontier Science Key Project of Chinese Academy of Sciences (QYZDJ-SSW-SLH038, Z. Y. T.), and K. C. Wong Education Foundation (Z. Y. T.).

References

1 Y. Hori, K. Kikuchi and S. Suzuki, *Chem. Lett.*, 1985, **14**, 1695–1698.
2 C. W. Li and M. W. Kanan, *J. Am. Chem. Soc.*, 2012, **134**, 7231–7234.
3 D. M. Weekes, D. A. Salvatore, A. Reyes, A. Huang and C. P. Berlinguette, *Acc. Chem. Res.*, 2018, **51**, 910–918.
4 D. Gao, R. M. Arán-Ais, H. S. Jeon and B. Roldan Cuenya, *Nat. Catal.*, 2019, **2**, 198–210.
5 J. Qiao, Y. Liu, F. Hong and J. Zhang, *Chem. Soc. Rev.*, 2014, **43**, 631–675.
6 D. T. Whipple and P. J. A. Kenis, *J. Phys. Chem. Lett.*, 2010, **1**, 3451–3458.
7 C. Costentin, M. Robert and J. M. Savéant, *Chem. Soc. Rev.*, 2013, **42**, 2423–2436.
8 K. P. Kuhl, T. Hatsukade, E. R. Cave, D. N. Abram, J. Kibsgaard and T. F. Jaramillos, *J. Am. Chem. Soc.*, 2014, **136**, 14107–14113.
9 J. P. Jones, G. Prakash, G. A. Olah and J. Isr, *Chem*, 2014, **54**, 1451–1466.
10 J. K. Nørskov, T. Bligaard, J. Rossmeisl and C. H. Christensen, *Nat. Chem.*, 2009, **1**, 37–46.
11 C. M. Lieber and N. S. Lewis, *J. Am. Chem. Soc.*, 1984, **106**, 5033–5034.
12 S. Dou, J. Song, S. Xi, Y. Du, J. Wang, Z.-F. Huang, Z. J. Xu and X. Wang, *Angew. Chem., Int. Ed.*, 2019, **58**, 1–6.
13 S. Meshitsuka, M. Ichikawa and K. Tamaru, *J. Chem. Soc., Chem. Commun.*, 1974, 158–159.
14 X. Zhang, Z. Wu, X. Zhang, L. Li, Y. Li, H. Xu, X. Li, X. Yu, Z. Zhang, Y. Liang and H. Wang, *Nat. Commun.*, 2017, **8**, 14675.
15 Y. Z. Chen, Z. U. Wang, H. Wang, J. Lu, S. H. Yu and H. L. Jiang, *J. Am. Chem. Soc.*, 2017, **139**, 2035–2044.
16 C. S. Diercks, Y. Liu, K. E. Cordova and O. M. Yaghi, *Nat. Mater.*, 2018, **17**, 301–307.
17 M. B. Solomon, T. L. Church and D. M. D'Alessandro, *CrystEngComm*, 2017, **19**, 4049–4065.
18 S. Dou, J. Song, S. Xi, Y. Du, J. Wang, Z.-F. Huang, Z. J. Xu and X. Wang, *Angew. Chem., Int. Ed.*, 2019, **58**, 4041–4045.
19 C. Zhao, X. Dai, T. Yao, W. Chen, X. Wang, J. Wang, J. Yang, S. Wei, Y. Wu and Y. Li, *J. Am. Chem. Soc.*, 2017, **139**, 8078–8081.
20 J. Albo, D. Vallejo, G. Beobide, O. Castillo, P. Casta Ço and A. Irabien, *ChemSusChem*, 2017, **10**, 1100–1109.
21 L. Ye, J. Liu, Y. Gao, C. Gong, M. Addicoat, T. Heine, C. Wçll and L. Sun, *J. Mater. Chem. A*, 2016, **4**, 15320–15326.
22 X. Kang, Q. Zhu, X. Sun, J. Hu, J. Zhang, Z. Liu and B. Han, *Chem. Sci.*, 2016, **7**, 266–273.
23 N. Kornienko, Y. Zhao, C. S. Kley, C. Zhu, D. Kim, S. Lin, C. J. Chang, O. M. Yaghi and P. Yang, *J. Am. Chem. Soc.*, 2015, **137**, 14129–14135.
24 I. Hod, M. D. Sampson, P. Deria, C. P. Kubiak, O. K. Farha and J. T. Hupp, *ACS Catal.*, 2015, **5**, 6302–6309.
25 C. W. Kung, C. O. Audu, A. W. Peters, H. Noh, O. K. Farha and J. T. Hupp, *ACS Energy Lett.*, 2017, **2**, 2394–2401.
26 Y. T. Guntern, J. R. Pankhurst, J. Vvra, M. Mensi, V. Mantella, P. Schouwink and R. Buonsanti, *Angew. Chem., Int. Ed.*, 2019, **58**, 2–10.
27 A. Morozan and F. Jaouen, *Energy Environ. Sci.*, 2012, **5**, 9269–9290.
28 X. Ding and B.-H. Han, *Angew. Chem., Int. Ed.*, 2015, **54**, 6536–6539.
29 W. Morris, C. J. Doonan, H. Furukawa, R. Banerjee and O. M. Yaghi, *J. Am. Chem. Soc.*, 2008, **130**, 12626–12627.
30 J. Han, P. An, S. Liu, X. Zhang, D. Wang, Y. Yuan, J. Guo, X. Qiu, K. Hou, L. Shi, Y. Zhang, S. Zhao, C. Long and Z. Tang, *Angew. Chem., Int. Ed.*, 2019, **58**, 2–8.
31 V. Bambagioni, C. Bianchini, J. Filippi, A. Lavacchi, W. Oberhauser, A. Marchionni, S. Moneti, F. Vizza, R. Psaro and V. Dal Santo, *et al.*, *J. Power Sources*, 2011, **196**, 2519–2529.
32 M. Cho, J. T. Song, S. Back, Y. Jung and J. Oh, *ACS Catal.*, 2018, **8**, 1178–1185.
33 Y. Zhao, C. Wang, Y. Liu, D. R. MacFarlane and G. G. Wallace, *Adv. Energy Mater.*, 2018, 1801400.
34 V. S. P. K. Neti, X. Wu, S. Deng and L. Echegoyen, *Polym. Chem.*, 2013, **4**, 4566–4569.
35 H. Liu, J. Chu, Z. Yin, X. Cai, L. Zhuang and H. Deng, *Chem*, 2018, **4**, 1696–1709.
36 N. Li, W. Lu, K. Pei and W. Chen, *RSC Adv.*, 2015, **5**, 9374–9380.
37 N. Han, Y. Wang, L. Ma, J. Wen, J. Li, H. Zheng, K. Nie, X. Wang, F. Zhao, Y. Li, J. Fan, J. Zhong, T. Wu, D. J. Miller, J. Lu, S.-T. Lee and Y. Li, *Chem*, 2017, **3**, 652–664.
38 S. Lin, C. S. Diercks, Y.-B. Zhang, N. Kornienko, E. M. Nichols, Y. Zhao, A. R. Paris, D. Kim, P. Yang, O. M. Yaghi and C. J. Chang, *Science*, 2015, **349**, 1208–1213.
39 J. Shen, R. Kortlever, R. Kas, Y. Y. Birdja, O. DiazMorales, Y. Kwon, I. Ledezma-Yanez, K. J. Schouten, G. Mul and M. T. Koper, *Nat. Commun.*, 2015, **6**, 8177.
40 Y. Chen and M. W. Kanan, *J. Am. Chem. Soc.*, 2012, **134**, 1986–1989.
41 S. Kapusta and N. Hackerman, *J. Electrochem. Soc.*, 1984, **131**, 1511–1514.
42 H. Wu, M. Zeng, X. Zhu, C. Tian, B. Mei, Y. Song, X.-L. Du, Z. Jiang, L. He, C. Xia and S. Dai, *ChemElectroChem*, 2018, 5(19), 2717–2721.

